1 # Characterization of Non-Gaussianity in the Snow
2 # Distributions of Various Landscapes

4 **Noriaki Ohara[1], Andrew D. Parsekian[1], Benjamin M. Jones[2], Rodrigo C. Rangel[1, 6],**
5 **Kenneth M. Hinkel[3], and Rui A. P. Perdigão[4, 5]**

6 [1]University of Wyoming, Laramie, WY, USA

7 [2]University of Alaska Fairbanks, Fairbanks, AK, USA

8 [3]Michigan Technological University, Houghton, MI, USA

9 [4]Meteoceanics Institute for Complex System Science, IUC Physics of Complex Coevolutionary
10 Systems & Fluid Dynamical Systems, Washington, DC, USA

11 [5]Synergistic Manifolds, Lisbon, Portugal

12 [6]Department of Earth Sciences, University of Toronto, Toronto, Ontario, Canada

14 Corresponding author: Noriaki Ohara (nohara1@uwyo.edu)

15 **Summary**

16 Snow distribution characterization is essential for accurate snow water estimation for water
17 resource prediction from existing in-situ observations and remote sensing data at a finite spatial
18 resolution. Four different observed snow distribution datasets were analyzed for Gaussianity. It
19 was found non-Gaussianity of snow distribution is a signature of wind redistribution effect.
20 Generally, seasonal snowpack can be well approximated by Gaussian distribution for fully snow-
21 covered area.

Abstract

Seasonal snowpack is an important predictor of available water resources in the following spring and early summer melt season. Total basin snow water equivalent (SWE) estimation usually requires a form of statistical analysis that is implicitly built upon the Gaussian framework. However, it is important to characterize the non-Gaussian properties of snow distribution for accurate large-scale SWE estimation based on remotely sensed or sparse ground-based observations. This study quantified non-Gaussianity using sample negentropy, the Kullback–Leibler divergence from Gaussian distribution, for field-observed snow depth data on the North Slope, Alaska, and three representative SWE distributions in the western US from the Airborne Snow Observatory (ASO). Snowdrifts around lakeshore cliffs and deep gullies can bring moderate non-Gaussianity in the open, lowland tundra of North Slope, Alaska, while the ASO dataset suggests that subalpine forests may effectively suppress the non-Gaussianity of snow distribution. Thus, non-Gaussianity is found in areas with partial snow cover and wind-induced snowdrifts around topographic breaks in slope and other steep terrain features. The snowpacks may be considered weakly Gaussian in coastal regions with open tundra in Alaska and alpine and subalpine terrains in the western US if the land is completely covered by snow. The wind-induced snowdrift effect can be potentially partitioned from the observed snow spatial distribution guided by its Gaussianity.

1 Introduction

Modeling of the spatial variability of snow is important for large-scale earth surface modeling since atmospheric circulation is sensitive to snow cover presence (e.g., Aas et al., 2016; Meng, 2017; Mott et al., 2015, 2017; Nitta et al., 2014; Younas et al., 2017). Since subgrid variability often causes appreciable bias in weather predictions (e.g. Lalande et al., 2023; Rudisill et al.,, 2024), accurate snow cover quantification can potentially improve the predictability of weather, planetary boundary-layer evolution, convective cloud formation, and even tropical cyclogenesis (Santanello et al., 2018). Hence, the subgrid variability of snow cover has been incorporated into operational regional weather forecasting models such as the High-Resolution Rapid Refresh (HRRR) model (He et al., 2021).

Observations of seasonal snow storage in mountainous areas through remote sensing and ground-based measurements are a direct and reliable indicator of the water supply during the following spring season in downstream regions (e.g. Fleming et al., 2023; Sengupta et al., 2022). However, total basin snow water equivalent (SWE) estimation usually requires a statistical relationship such as the snow depletion curve (SDC), which correlates with observables such as the snow cover area fraction (SCF). Based on a study of the observed snow distributions in Reynolds Creek Experimental Watershed in Idaho, Luce et al. (1999) showed that one snow distribution can reasonably represent the SDC evolution for the rest of the season. Also, Luce and Tarboton (2004) showed a high degree of similarity in nine years of dimensionless depletion curves measured in the same basin. Shamir and Georgakakos (2007) demonstrated the consistency of SDC over a season in the American River using a distributed model. The subseasonal and

62 interseasonal consistency in SDCs suggests the possibility for subgrid snow characterization as
63 well as basin wide SWE estimation from SCF data such as the MODIS product (Hall et al.,
64 2006).

65 As remote sensing technologies advance, seasonal snow distribution characterization becomes
66 more approachable with multi-sensor methods. For example, Tarricone et al. (2023) analyzed
67 three Interferometric Synthetic Aperture Radar (InSAR) image pairs to assess SWE evolution
68 using the snow-focused multi-sensor method with Uninhabited Aerial Vehicle Synthetic
69 Aperture Radar (UAVSAR) and an L-band InSAR data as well as optical fractional snow-
70 covered area (SCA) information. However, to estimate the total basin SWE in water resource
71 management practices, statistical empirical relationships are required to fill gaps in the spatial
72 and temporal resolutions—even when using these remote sensing observations (Tsang et al.,
73 2022). For example, Meloche et al. (2022) assumed log-normal distribution to represent the sub-
74 pixel variability of remotely sensed data. Thus, uncertainty and subgrid variability must be
75 accounted for when using statistical characterization in SWE estimation.

76 The most popular choice for the probability density function (PDF) of snow is log-normal
77 distribution, which inherently eliminates negative snow depth (Donald et al., 1995; Liston, 2004;
78 and many others). Brubaker and Menoes (2001) chose a beta distribution, while Kolberg and
79 Gottschalk (2006) selected a two-parameter γ-distribution. Although these common distributions
80 are in the exponential family, they were primarily chosen for convenience. Indeed, the
81 representativeness of these parametric probability distributions remains questionable for different
82 landscapes and snowpack ages (e.g., Skaugen & Randen, 2013; Egli & Jonas, 2009; He, Ohara,
83 & Miller, 2019). Moreover, these approaches for bounded distributions may not work for
84 evolving snowpacks with partial SCA where zero values are present in the probability domain.

85 In theory, without microtopography and meteorological effects, since the landing location of
86 each snow particle fallen from the atmosphere is considered an independent and identically
87 distributed (iid) random variable, the resulting snow depth or SWE distribution should
88 asymptotically approach a Gaussian distribution due to the central limit theorem. He, Ohara, and
89 Miller (2019) reported non-Gaussian snow distribution in open areas as well as Gaussian snow
90 distributions in the forested, fully snow-covered areas during the peak snow season using
91 airborne Light Detection and Ranging (LiDAR) observations in the Snowy Range, Wyoming.
92 This implies the presence of both systematic (non-Gaussian) and random (Gaussian) mechanisms
93 in snow accumulation and ablation processes. Therefore, it is possible to identify the potential
94 factors as "signals" that make the snow distribution deviate from a Gaussian distribution by
95 analyzing the resultant snow distributions.

96 This study applies negentropy to analyze the non-Gaussianity of snow distributions in Arctic
97 tundra, as well as alpine and subalpine landscapes in North America. Negentropy measures the
98 departure in entropy between a sampled distribution and Gaussian distribution of identical
99 variance and mean. Signals of interest (e.g., systematic snowdrift patterns) can be extracted as
100 non-Gaussian components because pure random noise asymptotically becomes Gaussian in
101 theory. This is the main idea of independent component analysis (ICA; Hyvärinen et al., 2000).
102 This work presents the quantified non-Gaussianity of the observed snow distributions through a

103 variety of snow distribution data, including intense direct hand measurements within 30-m grids
104 using a probe, and indirect measurements using a snowmachine-attached ground-penetrating
105 radar (GPR), UAV-based photogrammetry, as well as the Airborne Snow Observatory (ASO)
106 SWE products.

2 Methods

2.1 Negentropy

109 To measure the non-Gaussianity of any data, we implement the information-theoretic metric of
110 negentropy as the objective function since negentropy is equal to the Kullback–Leibler
111 divergence between p_x and a Gaussian distribution with the same mean and variance as p_x.
112 There is a well-known proposition that Gaussian density has the largest information entropy
113 among all unbounded distributions with the same first and second-order statistics. As such, the
114 non-Gaussianity of an observed distribution can be quantified by negentropy J, which is defined
115 as follows (Hyvärinen et al., 2000):

$$J(X) = S(X_{gauss}) - S(X) \tag{1}$$

117 where S is the information entropy of X. The information entropy can assume a diversity of
118 metrics ranging from the most general capturing microphysical event-scale codependence in
119 nonlinear statistical mechanics (Perdigão 2018) or simply assuming basic event-scale
120 independence in classical information theory (Shannon (1948) statistical entropy). For the
121 purpose of this study, we take the latter simple form, which is defined as:

$$S(X) = - \int p_x(\eta) \log[p_x(\eta)]d\eta, \tag{2}$$

123 where p_x is the PDF of X, and η is a dummy variable for the integration. The Edgeworth
124 expansion (Edgeworth, 1905) can provide an approximation for a PDF of X, as follows:

$$p_x(X) = \frac{\phi(U)}{\sigma}\left[1 + \frac{\kappa_3}{6}H_3(U) + \frac{\kappa_4}{24}H_4(U) + \frac{\kappa_3{}^2}{72}H_6(U) + \cdots\right] \tag{3}$$

126 where

127 $\qquad U$ = standardized random variable of X

128 $\qquad H_k(U)$ = Chebyshev-Hermite polynomials

129 $\qquad \phi(U)$ = standard normal density

130 $\qquad \kappa_k$ = k-th order cumulant of U.

131 Substituting the Edgeworth series into the negentropy definition, Comon (1994) obtained the
132 analytical expression:

$$J(X) = \frac{1}{12}\kappa_3{}^2 + \frac{1}{48}\kappa_4{}^2 + \frac{7}{48}\kappa_4{}^4 - \frac{1}{8}\kappa_3{}^2\kappa_4 + O(n^{-2}). \tag{4}$$

134 This is the estimator of negentropy at fourth-order cumulant. In practice, a more intuitive
135 approximation is commonly used, as follows:

136 $$J(X) = \frac{1}{12}\text{skew}(U)^2 + \frac{1}{48}\text{kurt}(U)^2 \tag{5}$$

137 where skew and kurt are the skewness and kurtosis of standardized variable, U, respectively.

138 The sample estimation of the higher-order moment and cumulant (e.g., skew and kurtosis
139 coefficients) is known to be sensitive to the presence of outliers. In this study, the interquartile
140 range (IQR) method was adopted for outlier removal with a minimum removal that lies outside
141 the range of three times IQR.

142 While negentropy metrics and corresponding Edgeworth approximations have been previously
143 explored and further developed in atmospheric sciences and in physics, including derivations and
144 implementations to higher-order distributions, elaborate numerical and analytical estimators
145 (Pires and Perdigão 2007, Perdigão 2010, Perdigão 2017), the present study brings a simplified
146 treatment not yet explored in hydrology and tailored for swift and seamless integration within
147 hydrological and water resource systems investigations.

148 **2.2 Data collection**
149 We analyzed four types of data with different collection methodologies at various scales in this
150 study, as listed in Table 1. The first is manual snow depth surveys using a GPS-aided snow probe
151 (Magnaprobe; Sturm & Holmgren, 2018), the second is snow depth transects using a
152 snowmachine-attached GPR, the third is snow depth maps using UAV-based photogrammetry,
153 and the last is the SWE product of the ASO. The first three datasets are for the open tundra in the
154 Arctic Coastal Plain (ACP) of Alaska while the ASO data are for the alpine and subalpine
155 regions of the continental USA. Detailed data specifications associated with the collection
156 methodologies will be presented in Results section below. Figure 1 displays the map of the snow
157 depth surveys in North Slope, Alaska, USA.
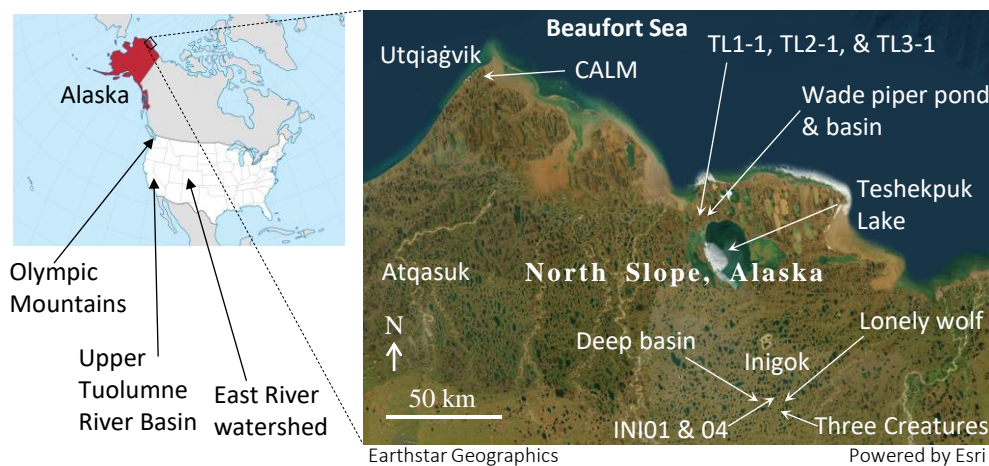
158

159 Figure 1: Map of the snow survey locations in Alaska, USA, and the selected ASO sites.

160

161 Table 1: List of snow datasets

Site name	Location	Lon/Lat	Spatial resolution	Elevation range	Data collection method	Date	Sample size	Landscape and land cover
TL1-1	Teshekpuk, AK	70.738°N, 153.970°W	~1m	0.91~1.20 m MSL	Magnaprobe	April 24, 2022	951	Open tundra, sedge and herbaceous
TL2-1	Teshekpuk, AK	70.740°N, 153.956°W	~1m	2.35~2.54 m MSL	Magnaprobe	April 25, 2022	925	Open tundra, sedge and herbaceous
TL3-1	Teshekpuk, AK	70.739°N, 153.928°W	~1m	1.86~2.18 m MSL	Magnaprobe	April 25, 2022	904	Open tundra, sedge and herbaceous
Wade piper pond	Teshekpuk, AK	70.751°N, 153.870°W	~1m	2.18~2.50 m MSL	Magnaprobe	April 27, 2022	927	Open tundra, sedge and herbaceous
Wade piper basin	Teshekpuk, AK	70.746°N, 153.854°W	~1m	3.68~3.88 m MSL	Magnaprobe	April 29, 2022	960	Open tundra, sedge and herbaceous
Inigok	Inigok, AK	70.001° N, 153.068°W	~0.5m	37.8~59.1 m MSL	GPR	May, 2019	16655	Open tundra, sedge and herbaceous
CALM	Utqiaġvik, AK	71.3026°N, 156.6008°W	0.25m	-1.93~3.8 m MSL	UAV photogrammetry	May, 2019	2,928,240	Open tundra, sedge and herbaceous
Upper Tuolumne River	California	37.461°N, 119.494°W	50 m	1,142~3,965 m MSL	ASO SWE product	April 3, 2013	470,213	Steep rocky alpine terrain, partially forested
East River	Colorado	39.037°N 106.978°W	50 m	2,343~3,901 m MSL	ASO SWE product	March 31, 2018	667,883	Alpine and subalpine forest
Olympic Mountains	Washington	47.792°N 123.650°W	50 m	0~2,432 m MSL	ASO SWE product	March 29, 2016	2,066,907	Dense forest and high peaks

162

3 Results

3.1 Manual snow surveys at Teshekpuk, North Slope, Alaska (May 2022)

164
165 Snow depth data were collected using a Magnaprobe (Sturm & Holmgren, 2018) in five 30 x 30-
166 m grids with 1 m grid spacing north of Teshekpuk Lake, North Slope, AK, in May 2022. The
167 GPS location of each measurement was automatically recorded. Figure 2 presents the
168 interpolated snow depth distributions and corresponding histograms (right columns) in five areas
169 near Teshekpuk. The observer measured the point scale snow depth at approximately every 1 m
170 along a line toward flags placed 1 m apart on the surface. Since the data points were selected
171 from undisturbed snow, the locations are unevenly distributed despite the snowpacks generally
172 being highly hardened by wind. The relative spatial locations are considered accurate since the
173 operator stood on the same side of the probe and followed pre-marked lines based on the tape
174 measure; however, the absolute plotted coordinate in the figures may not be trustworthy due to

175   the GPS horizontal accuracy < 3 m. The topography of these grids in the ACP are very flat with

176   elevation variation of less than 1 meter while accurate absolute elevation data are hard to

177   compare due to the spatial inaccuracy of the Magnaprobe.

178   The graphics in the left column of Figure 2 present the point depth observation locations and

179   interpolated snow depth distributions using the nearest distance method. The number of data

180   points denoted by the black dots is n=951 (TL1-1), n=925 (TL2-1), n=904 (TL3-1), n=927

181   (Wadepiper Pond), and n= 960 (Wadepiper Basin).

182   The corresponding snow depth histograms and three fitted distributions are displayed in the right

183   column. The statistics mean, standard deviation, skew coefficient, and negentropy (J) are

184   reported on the top part of each graph. In general, the snow depth distributions in these areas are

185   almost Gaussian distributions since the computed negentropy is small. However, the negentropy

186   of snow distribution affected by wind-induced snowdrift (sastrugi) on frozen lakes is larger than

187   the tundra covered by sedge and herbaceous vegetation. In practice, the non-Gaussianity of

188   seasonal snow depth may have been negligible in the coastal open tundra (including frozen open

189   waters) in the Teshekpuk study area in May 2022.

190
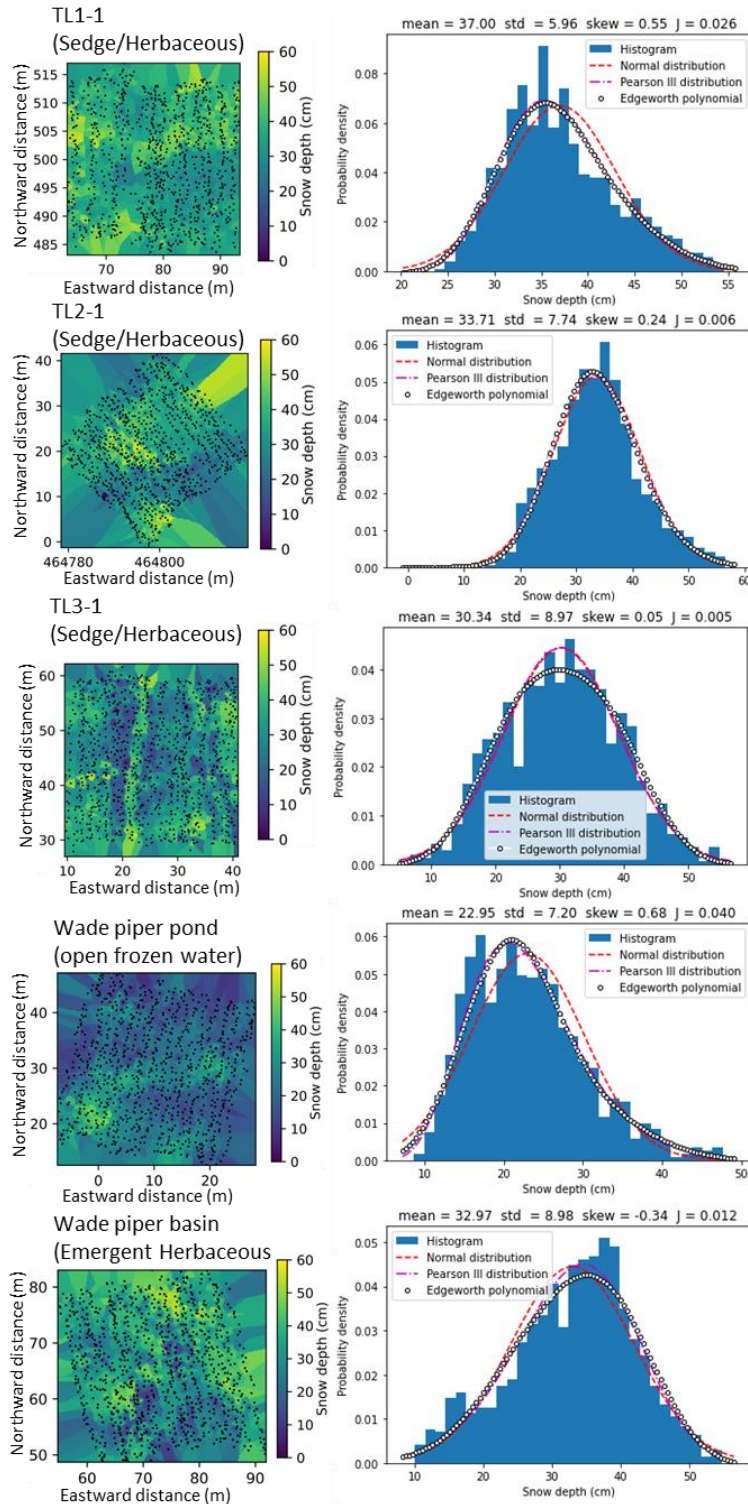
Figure 2: Manual snow distributions in the Teshekpuk Lake area, North Slope, Alaska (May
2022) and corresponding histograms with fitted probability density functions (PDFs). *J* denotes
the computed negentropy. Snow depth histograms in open tundra in 30 m x 30 m squares are
generally categorized as "weak-non-Gaussian." The approximated center coordinates of the grids

195 are 70.738°N, 153.970°W (TL1-1), 70.740°N, 153.956°W (TL2-1), 70.739°N, 153.928°W (TL3-
196 1), 70.751°N, 153.870°W (Wadepiper Pond), and 70.746°N, 153.854° W (Wadepiper Basin).

3.2 Snow depth surveys using GPR along multiple transects in Inigok, North Slope, AK (April 2019)

199 The Inigok area of North Slope, Alaska (70.001° N, 153.068° W) is characterized by paleo sand
200 dunes (Carter, 1981), hydro-geomorphological processes, and permafrost landforms such as
201 thermokarst lake formation and drainage. The landscape is characterized by relatively steep
202 terrain and substantial wind-induced snowdrifts (deeper than 5 m), especially around lake shores
203 and drainage channels (e.g., Rangel et al., 2023).

204 Snow depth surveys using a GPR are particularly effective for deep-snow areas since the
205 Magnaprobe is only 1.5 m long. Considering the lower limit of the selected GPR antenna, we
206 collected several GPR transects (Malå ProEx, 800 MHz, GuidelineGeo, Sundbyberg, Sweden)
207 around Inigok, where the snowpack was deeper than in the coastal area. The antenna was placed
208 on a sled towed by a snowmachine traveling < 5km h^{-1}. The effect of compaction by the
209 snowmachine was considered negligible because the snow was highly wind-packed and therefore
210 was not affected by the weight of the snowmachine during data collection. The GPR data were
211 processed in ReflexW (Sandmeier Software, Karlsruhe, Germany) using a low frequency noise
212 removal (dewow) and a linear gain with topographic correction adapted from the ArcticDEM
213 (Rangel et al., 2023b). Maps of snow depth estimated from the GPR transects are shown in
214 Figure 3. The line color denotes the observed snow depth (the darker, the deeper). A substantial
215 snowdrift developed near the lakeshore's banks due to its steep topography.

216 Figure 4 displays the histograms of GPR snow depth data in Inigok, North Slope, Alaska, in May
217 2019 when using (A) all transect data and (B) the frozen lake sections only. The snow depth
218 histogram of all transects shows strong non-Gaussianity due to a mix of steep and flat terrain.
219 However, the histogram of the partial dataset only for the frozen lakes shows much weaker non-
220 Gaussianity. In fact, snow distribution after removing the deep-snow parts can be reasonably
221 approximated by the Gaussian distribution with a negentropy of 0.037, which is the same level as
222 Wadepiper Pond (Figure 2) in the previous section (J = 0.040). Therefore, the snowdrift due to
223 steep terrain is considered a major source of non-Gaussianity in snow depth in open tundra.
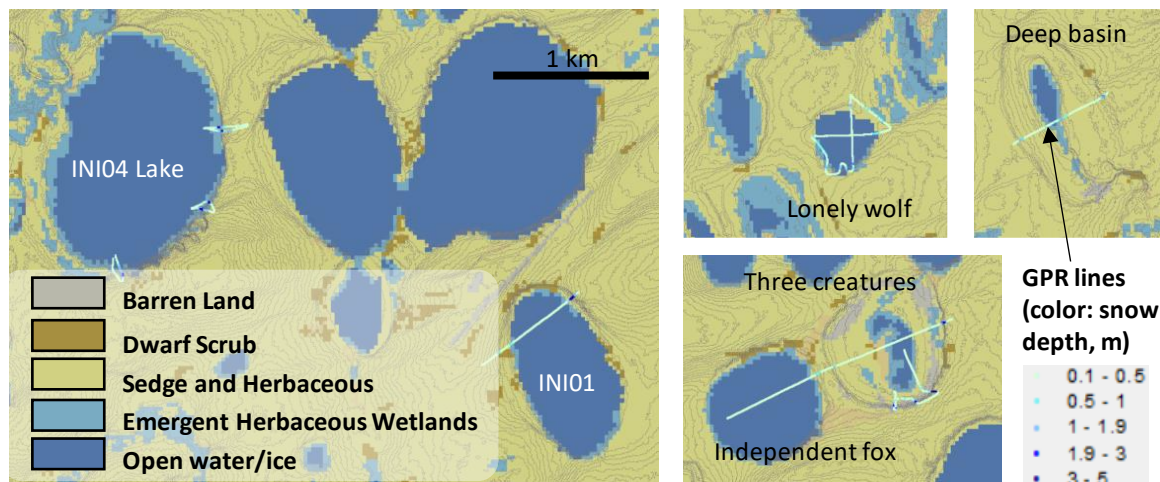
224

225 Figure 3: Snow depth surveys using GPR along multiple transects in Inigok, North Slope, Alaska
226 (27 and 28 April 2019) superimposed over the land cover map with 1 meter interval contour
227 lines. The approximated center coordinates of the maps are 153.105W 70.005N (INI04 &
228 INI01), 152.949W 69.993N (Lonely wolf), 153.274W 69.992N (Deep basin), and 153.032W
229 69.942N (Three creatures & Independent fox).
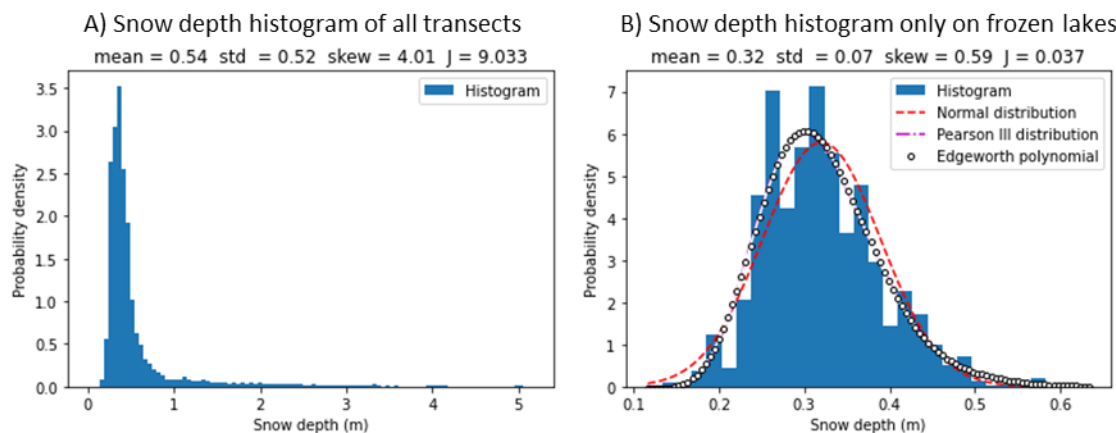
230

231 Figure 4: Snow depth histograms of GPR snow survey data from Inigok, North Slope, Alaska
232 (April 2019) using A) all transects and B) sections on frozen lake only. Snow distributions in the
233 Inigok area are highly non-Gaussian, while the frozen lake subset shows weak non-Gaussianity.

234

3.3 Snow depth distribution based on UAV footage of a drained lake basin within the CALM 1-km grid near Utqiaġvik, AK (May 2019)

237 Figure 5 (left panel) presents the observed snow distribution of a drained thermokarst lake basin
238 referred to as Central Marsh, part of the Circumpolar Active Layer Monitoring (CALM)
239 Network located east of Utqiaġvik, Alaska. The snow depth was estimated by differentiating the
240 snow surface elevation and the snow-free ground elevation using UAV surveys with the
241 photogrammetry technique. The images were collected on August 4, 2019 (snow-free), and April
242 15, 2019 (snow-covered), using a Phantom 4 UAV (P4RTK). Images were post-

243 processed/georeferenced to NAD83 Zone 4 North in ellipsoid heights using a propeller aeropoint
244 and Pix4D (version 4.3.33 for the April survey, 4.4.12 for the August survey) at 0.25 m spatial
245 resolution (Nichols, 2020). The vertical accuracies of these measurements are 18 cm and 10 cm
246 for the April and August surveys, respectively. The horizontal resolution for the snow depth is 1
247 m.

248 The CALM site is situated in the ACP in northern Alaska, which has typical complex terrain due
249 to the recently drained thermokarst lake with sparse or negligible vegetation and well-developed
250 polygons. There is an obvious smoothed bluff in the center of the domain, and the west side of
251 this bluff tapers into the drained lake basin. The incised drainage channels cause steep land
252 features that capture sizable snowdrifts in the southern part. In the southern portion of the area,
253 the polygons are formed by ground surface cracks with ice wedge development beneath found in
254 lower and higher center parts in the left panel of Figure 5.

255 The negentropy distribution in the moving window may be obtained from this gridded snow data
256 at a very high spatial resolution. The right panel of Figure 5 presents the computed negentropy
257 map in the CALM area with a 30-m moving window. Overall, non-Gaussianity in the CALM site
258 was found to be weak—even with the smoothed bluff and despite high snow depth. However, as
259 whiter parts in right panel of Figure 5 are found along the drainage channels, topographic
260 discontinuity around the incised gully seems to cause significant non-Gaussianity. Additionally,
261 vegetation patches may bring spotty non-Gaussianity in the northern part of the area. Conversely,
262 since the southern parts covered by the polygons except the drainage channels show darker color
263 (J <0.025), the ground surface polygon does not make snow distribution non-Gaussian. Overall,
264 snowpack in the coastal parts of the ACP can reasonably be approximated by Gaussian
265 distribution since most of the CALM area showed a small negentropy of less than 0.2.
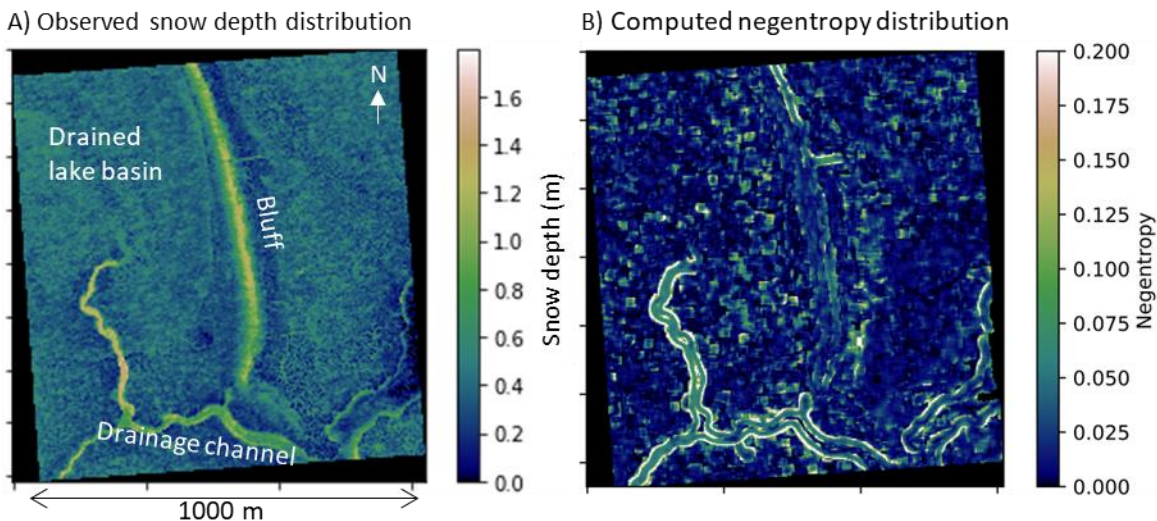
266

267 Figure 5: Snow depth distribution based on UAV photogrammetry and the computed negentropy
268 distribution of 30-m moving windows in a drained lake basin in the CALM 1-km grid (71.3026°
269 N, 156.6008°W) near Utqiaġvik, Alaska.

270 Figure 6 presents the snow depth histogram, which looks like a Gaussian distribution with a long
271 tail due to snowdrift around the gullies in the CALM grid. In fact, when the deep snowdrifts of
272 the gully and the bluff are removed from the samples, the histogram more closely resembles a
273 Gaussian distribution (see the right panel in Figure 6).
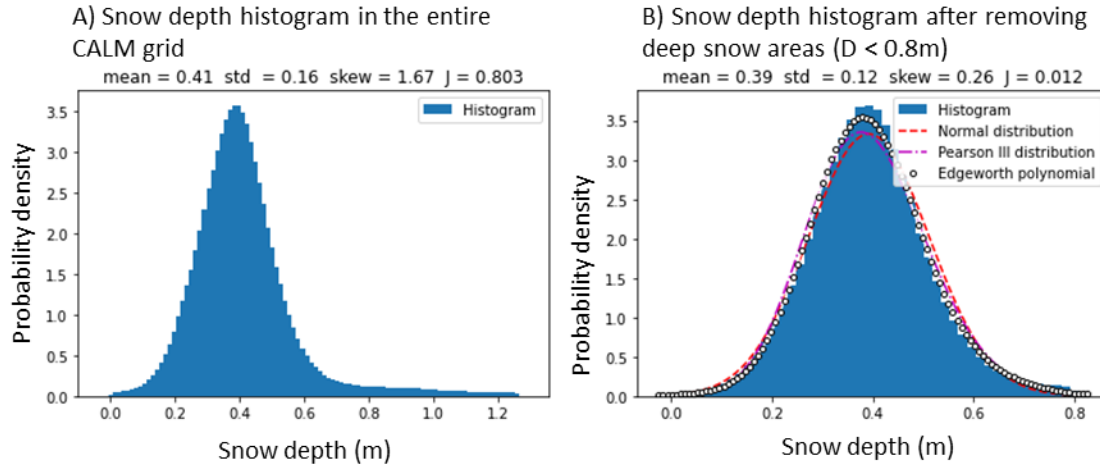
274

275 Figure 6: Snow depth histogram based on the UAV photogrammetry of a drained lake basin in
276 the CALM 1-km grid near Utqiaġvik, Alaska. Removing the deep snow parts caused by wind-
277 induced snowdrift results in a near-perfect fit by Gaussian distribution.

278 **3.4 SWE products based on ASO data for the selected watersheds**
279 SWE is a stable and direct indicator of snow/water distribution in landscapes. As such, the SWE
280 products from the Airborne Snow Observatory (ASO) were selected (Painter et al., 2016) to
281 examine the Gaussianity of snow distributions in different climate zones and landscapes with
282 alpine to subalpine snowpack. The snow depth and SWE distributions were estimated from the
283 coupled imaging spectrometer and scanning LiDAR, then combined with distributed snow
284 modeling (including snow density simulation). The ASO snow products are considered one of
285 the most comprehensive instantaneous snow distribution estimations at fine resolution (50 m).
286 We used the processed snow product to characterize the medium-scale snow distribution with the
287 same outlier treatment (IQR method) as described above.

288 The analysis of three representative SWE datasets in the western US is presented. These include
289 Upper Tuolumne River watershed in California (USCATB, April 3, 2013), East River watershed
290 above Gunnison, Colorado (USCOGE, March 31, 2018), and the Olympic Mountains in
291 Washington (USWAOL, March 29, 2016).

292 **3.4.1 Tuolumne River Watershed, California**
293 Figure 7 presents the composite graphics of the data and the analysis results for the Upper
294 Tuolumne River watershed on April 3, 2013. Panel A shows the SWE distribution estimated by
295 the ASO, while panel B visualizes the normalized SWE histogram or PDF within the entire
296 domain with the fitted theoretical distributions. Panels C and D are the negentropy distributions
297 of the SWE within 1500-m moving windows with and without partially snow-covered cells.
298 Panel E shows the NLCD 2011 land cover map for reference. The watershed (1175 km^2) is one

299   of the drainages to the California Central Valley through the Hetch Hetchy reservoir in the
300   southern Sierra Nevada Mountain Range. The boundary of the catchment is mostly comprised of
301   steep rocky alpine terrain (which contributes to the attractive land features of Yosemite National
302   Park), whereas the bottom of the valley is relatively flat due past glacial processes. The snow
303   distribution (panel A) shows a clear relationship with elevation, while the SWE barely exceeded
304   1 m during the observation period in peak snow season. The overall SWE histogram (panel B)
305   illustrates strong non-Gaussianity because of snow-free and shallow accumulation areas in the
306   watershed (bounded distribution effect).

307
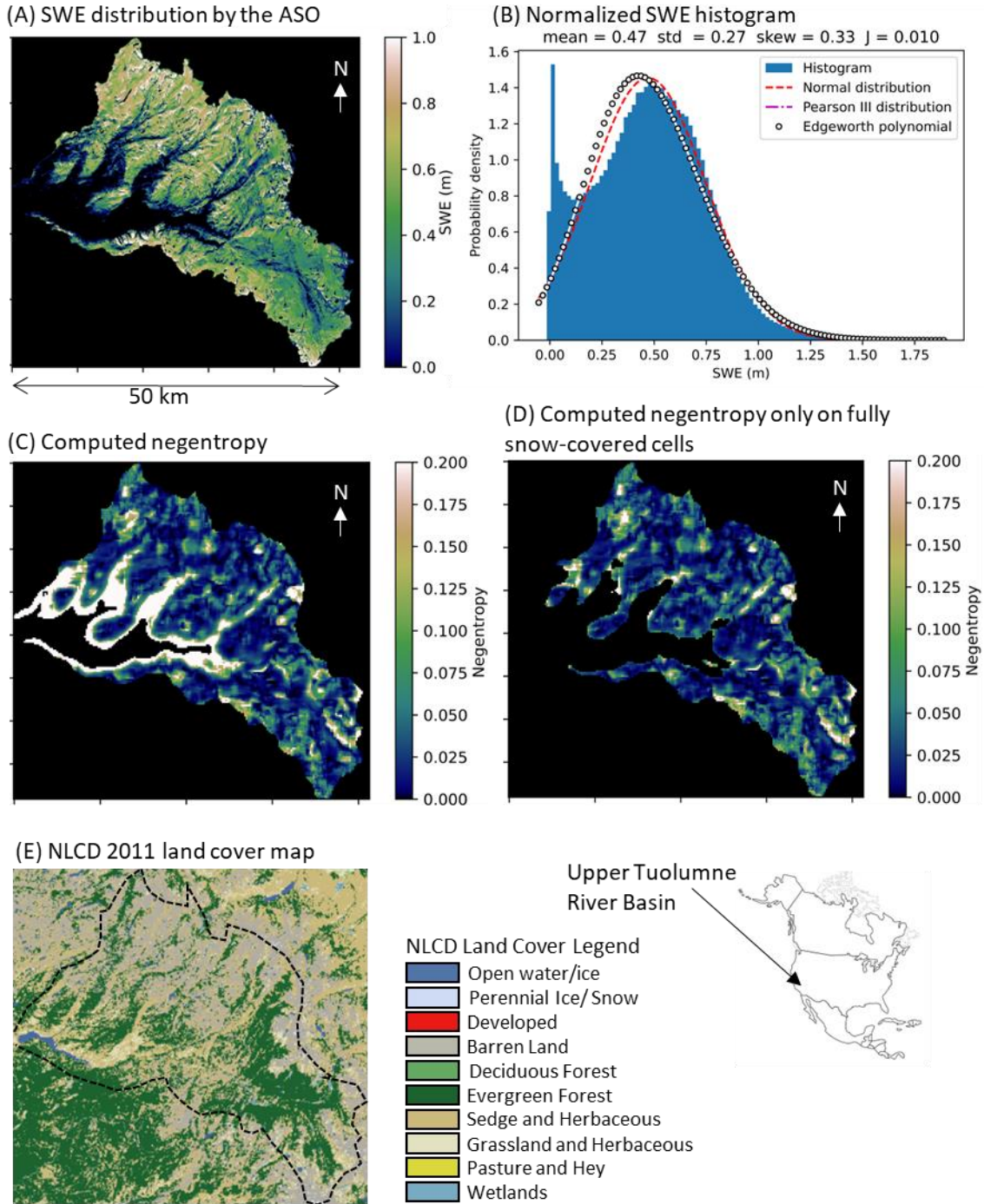
Figure 7: (A) SWE distribution based on ASO data of the Upper Tuolumne River Basin, California, USA from April 3, 2013 (USCATB, 37.461°N, 119.494°W); (B) normalized SWE histogram; (C) negentropy map of the SWE within 1500-m moving windows; (D) negentropy map of only fully snow-covered cells; (E) NLCD 2011 land cover map.

However, the local negentropy map with moving windows (panel C) shows small non-Gaussianity except in the low-elevation areas. In fact, the majority of high non-Gaussianity cells are from partially snow-covered cells. When the partially snow-covered cells are removed in

315   panel D, the local negentropy falls by less than 0.15 in most of the watershed. Therefore, the
316   bounded distribution effect in the probability domain from the partially snow-covered cells
317   brings substantial non-Gaussianity into the snow distribution.

318   Additionally, the spatial resolution of 50 m may be too coarse to capture the local snowdrift
319   effect discussed in sections 3.2 and 3.3. using the very fine resolution data since snowdrift extent
320   around steep cliff is often smaller than the resolution of medium to large scale snow products.
321   Therefore, even with fully snow-covered areas, fine resolution data is required for snowdrift
322   characterization which is potentially important for more accurate snow storage estimation.
323   However, further study is recommended using finer resolution snow data although the combined
324   effect of steep terrain and vegetation on snowdrift is highly complicated and hard to characterize
325   even with modern remote sensing technology.

326   **3.4.2 East River, Colorado**
327   The ASO dataset of the East River above Gunnison, Colorado (USCOGE) was selected as a
328   representative basin in the Rocky Mountains region. This dataset includes the U.S. Department
329   of Energy (DOE)'s East River community observatory, where comprehensive field data have
330   recently been collected (Kakalia et al., 2020). The data domain, which does not agree with the
331   watershed boundary, is approximately 1670 km^2 with the elevation ranging from 2,343m
332   (Gunnison) to 3,901 m. Figure 8 displays the corresponding analysis results of the East River
333   area on March 31, 2018.

334
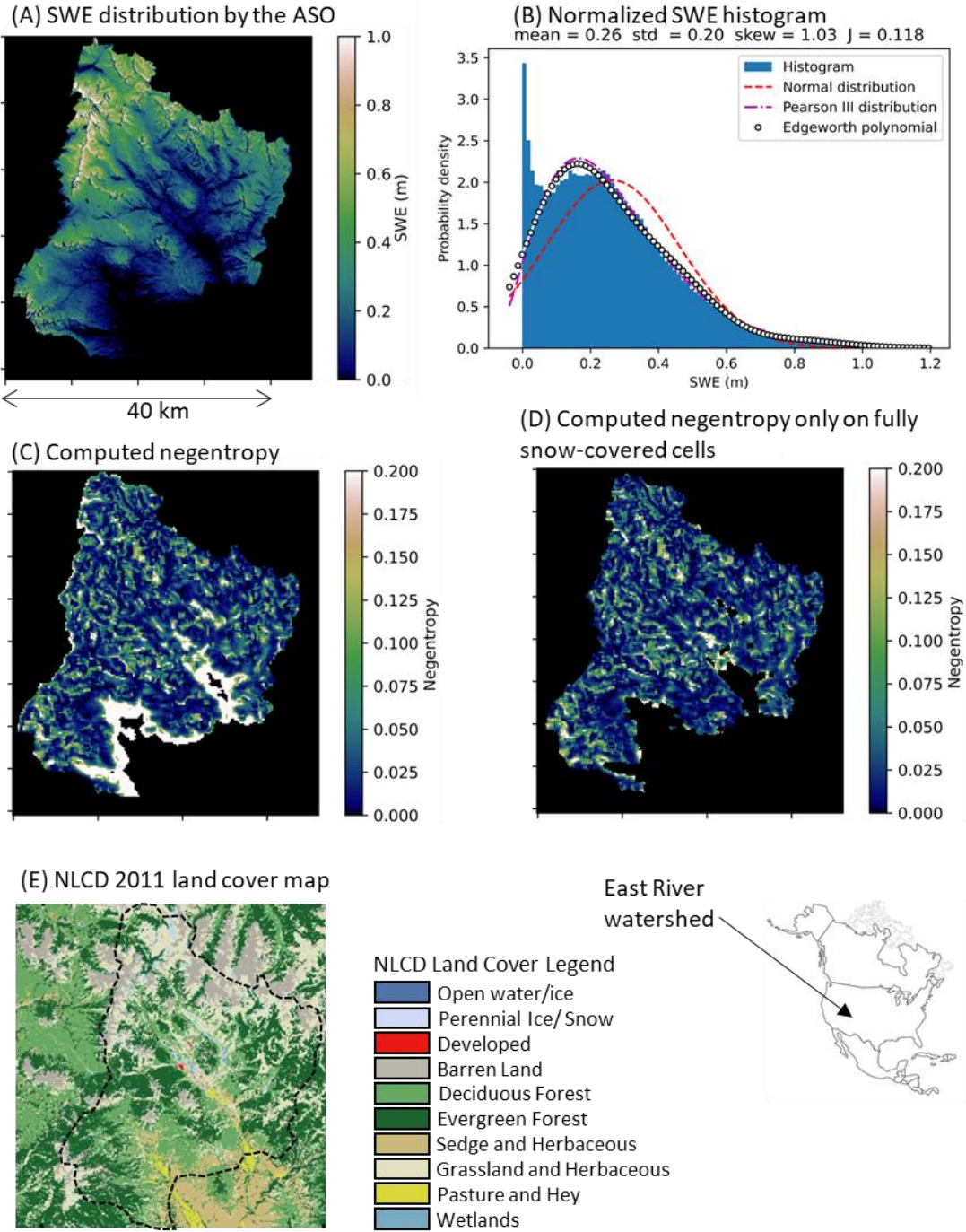
Figure 8: (A) SWE distribution based on ASO data for the East River watershed above
Gunnison, Colorado, USA from March 31, 2018 (USCOGE, 39.037°N 106.978°W); (B)
normalized SWE histogram; (C) negentropy map of the SWE within 1500-m moving windows;
(D) negentropy map of only fully snow-covered cells; (E) NLCD 2011 land cover map.

Besides the obvious bounded distribution effect of partially snow-covered cells, this case study
illustrates the non-Gaussianity induced by the steep topographic features around the high peaks
in the Rocky Mountains. However, it is interesting that the range of negentropy remains less than

342 0.5 in fully snow-covered areas in panel D despite very steep topography in the East River
343 watershed. At Inigok, for example, it is a flat/low-rolling-hills landscape that is punctuated by
344 very abrupt, very steep bluffs that cause the large drifts. In contrast, while East River certainly
345 has much more total topographic relief, it does not have the same long, flat fetch area where the
346 wind can build unimpeded, nor does it have similar abrupt erosional bluffs. Also, since the lower
347 negentropy (darker colored) parts in panel D generally agree with the evergreen and deciduous
348 forest cover extent in the NLCD land cover map in panel E, the subalpine forest may reduce non-
349 Gaussianity in snow distribution. However, the general characteristics of the sample's
350 negentropy distribution in Upper Colorado are consistent with the Upper Tuolumne River
351 watershed in the Sierra Nevada Mountain Range.

352 **3.4.3 Olympic Mountains, Washington**
353 The last example of snow non-Gaussianity quantification is the Olympic Mountains in
354 Washington, USA, which represent the Northern Pacific Coastal Range under strong oceanic
355 influence. The elevation ranges from sea level to 2430 m. The Olympic Mountains consist of a
356 cluster of steep-sided peaks, heavily forested foothills, and incised deep valleys. The ASO data

357 have a large spatial coverage (5,330 km^2) when compared to the other two ASO datasets
358 presented here.
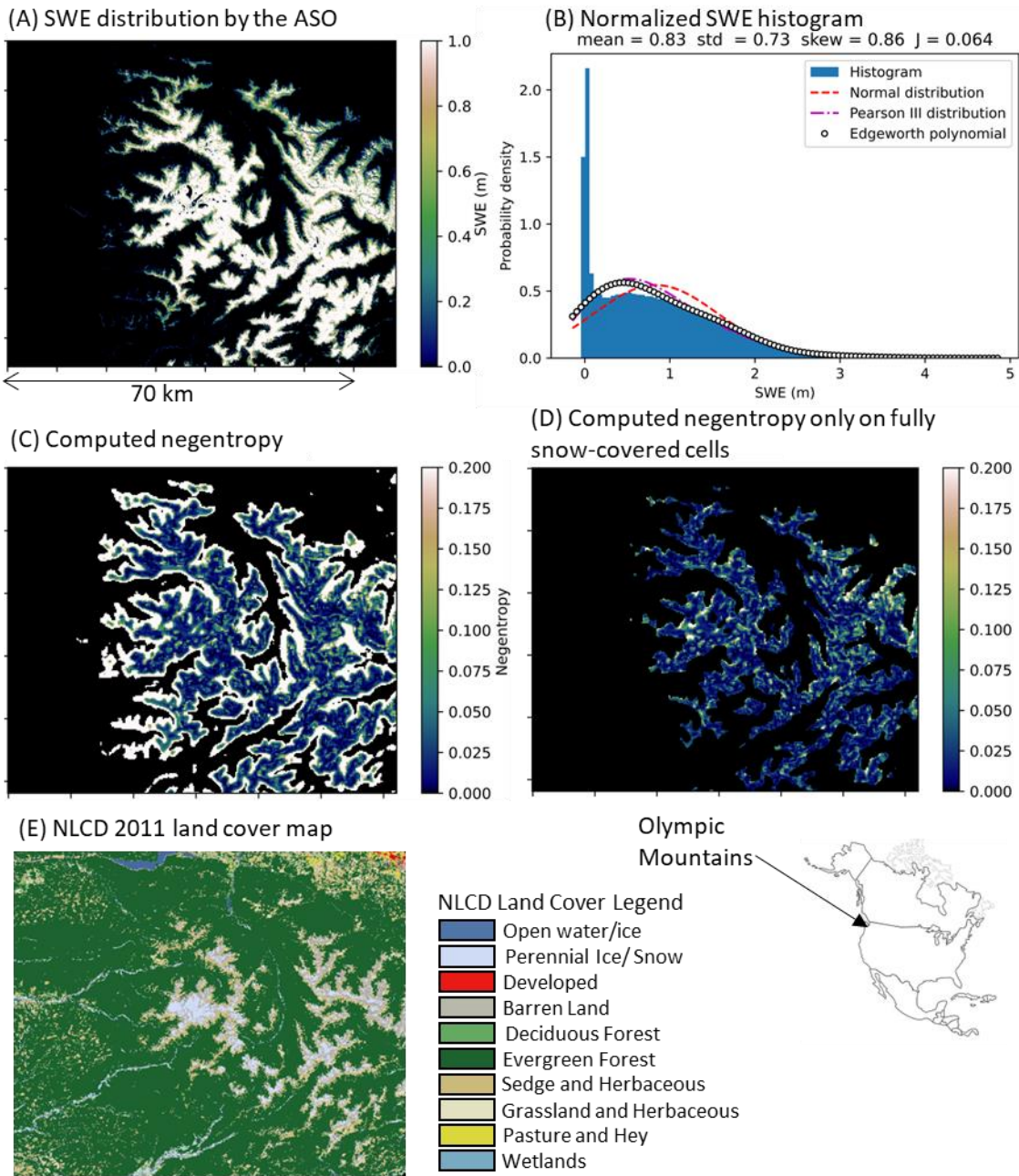
360 Figure 9: (A) SWE distribution based on ASO data for the Olympic Mountains, Washington,
361 USA from March 29, 2016 (USWAOL, 47.792°N 123.650°W); (B) normalized SWE histogram;
362 (C) negentropy map of the SWE within 1500-m moving windows; (D) negentropy map of only
363 fully snow-covered cells; (E) NLCD 2011 land cover map.

364 The black areas in the high elevation range in panel A are the approximate glacier extent
365 excluded from the analysis (Painter et al., 2018). A large fraction of partially snow-covered cells
366 also introduces non-Gaussianity in SWE in this region. Meanwhile, dense evergreen forests in

367 the Olympic Mountains seem to effectively reduce the non-Gaussianity of SWE above the snow
368 line during the ASO scanning period. Overall the non-Gaussianity of the snowpack may be
369 considered small when compared to the other two examples, which is likely due to denser forest
370 cover. Presumably, the vegetation cover minimizes the wind-induced snow redistribution process
371 and makes the snow distribution more Gaussian. These characteristics—i.e., non-Gaussianity in
372 partially snow-covered areas and high Gaussianity in forested areas—are common features of the
373 SWE distributions throughout the western US.

4 Discussion

375 The sample negentropy values presented here are generally consistent with each other despite the
376 variety of data collection methods used at different scales. The level of random noise in the
377 datasets depends on the data collection methods. Among the datasets discussed here, one may
378 anticipate that the ASO data have the largest Gaussian bias due to multiple remote sensing,
379 resampling, assimilating, and modeling procedures covering remarkable spatial coverages with
380 uniform data quality. The UAV-based LiDAR data at the North Slope CALM site are expected
381 to have a noticeable random bias with a vertical accuracy of approximately 12 cm. The GPR
382 snow depth observations should have a smaller but appreciable Gaussian bias due to snow
383 quality variation and non-flat snow surface elevation (antenna angle vibration), although the
384 continuous measurement minimizes the random relative error in the snow depth estimation. The
385 hand-measured snow depth data using a probe may include the least Gaussian bias, while the
386 sampling spacing was not uniform and in addition, due to relative poor spatial positioning
387 control with the Magnaprobe's onboard GPS unit. Despite these differences, it is encouraging
388 that the quantified Gaussian levels were comparable and consistent since they share common
389 features.

390 The stability of the sample estimator of negentropy may be a potential issue, especially when the
391 sample size is small. Additionally, since the higher-order statistical moments are sensitive to the
392 presence of outliers in the sample, an outlier removal filter is recommended for large samples.
393 The IQR method with a threshold of 3 IQR above the third quarter (Q3), which is stricter than
394 the usual threshold (typically 1.5 IQR), has been applied for the UAV photogrammetry data and
395 the ASO datasets for computational stability. Even with the large threshold (small outlier
396 removal), the proposed method using negentropy appears to be effective in characterizing the
397 Gaussianity of snow distribution, which has been a common implicit assumption for existing
398 gridded data and models. This study visualized the limitation of such a common distribution
399 assumption for snow distribution, specifically for areas with partial snow cover.

400 To summarize the analyses presented here, five categories of Gaussianity were defined and
401 associated with a magnitude of sample negentropy value (see Table 2). Most of the fully snow-
402 covered areas fell into the category "almost Gaussian," with a negentropy less than 0.03.
403 Notably, a negentropy less than 0.01 is considered nearly perfect Gaussian, as can be seen in the
404 previous sections.

405 The Gaussianity characterization of snow distribution appears to be useful in distinguishing the
406 snowdrift-affected areas using the sample negentropy. Simultaneously, this finding can justify

407 the implicit Gaussian assumption for snow distribution for overall SWE estimation, particularly
408 for snowpack characterization from remotely sensed information. For instance, the effect of
409 higher-order statistical moments can be negligible in most fully snow-covered areas. Conversely,
410 some additional statistical treatment for higher order statistics may be required for the areas with
411 the non-Gaussian effects around snow lines, open wind-swept areas, and sharp terrains.
412 Additionally, since consistent pattern in skew coefficient was not identified from the snow
413 datasets, the commonly-used log-normal distribution may not be suitable for those areas.

414 Table 2: Summary of the analysis using the sample negentropy.

Class	Negentropy	Landscape & land cover type	Examples
Strong non-Gaussian	$0.2 < J$	Partially snow-covered areas, mixture of landscapes (steep-flat)	CALM, Inigok, Upper Tuolumne, East River, Olympic Mountains
Non-Gaussian	$0.1 < J \leq 0.2$	Snowdrift around steep terrain	CALM
Weak non-Gaussian	$0.03 < J \leq 0.1$	Snowdrift on a frozen lake, vegetation cluster	Teshekpuk, Inigok, CALM
Nearly Gaussian	$0.01 < J \leq 0.03$	Most of the uniform terrain in open tundra and alpine forest	Teshekpuk, CALM, Upper Tuolumne, East River, Olympic Mountains
Gaussian	$J \leq 0.01$	Open tundra (sedge, polygons), most forested areas	Teshekpuk, Upper Tuolumne, East River, Olympic

415

416 It is encouraging that snow depth and SWE distributions are generally well approximated by the
417 Gaussian or weak non-Gaussian distribution, which is a fundamental assumption for statistical
418 characterization of sub-gird variability used in snowpack estimation by remote sensing. The non-
419 Gaussianity found in the partially snow-covered areas may also be modeled by truncated normal
420 distribution although it must be tested further. Moreover, weak non-Gaussian distribution would
421 enable the Edgeworth expansion method proposed by Pires and Perdigão (2007). For instance,
422 the non-Gaussian asymptotic method or information metric can effectively determine the saddle
423 point approximation of the joint probability density functions (PDF) through maximizing the
424 Shannon entropy between the remotely sensed signal and the SWE. Thus, the quantification of
425 non-Gaussiany in snow depth/SWE distributions would be an important milestone toward
426 accurate snow water quantification using remote sensing techniques as well as grid-based snow
427 and earth surface models.

5 Conclusions

A Gaussian snow distribution is a common underlying assumption for finite scale models or gridded datasets. The present study tested this assumption using the sample negentropy of various snow data. We found two main sources of non-Gaussianity: (1) partial snow cover effect (bounded distribution) and (2) wind-induced snowdrift effect around steep terrain features. The second effect may amplify the first one in wind-swept alpine areas since snow erosion remains shallow on rocky ridges and peaks. The snowdrift around lakeshore cliffs and deep gullies can bring moderate non-Gaussianity in the open tundra of North Slope, Alaska. However, the wind-packed snow in the coastal plain region of the North Slope may generally be categorized as weakly Gaussian during mid to late winter due to the continuous snow cover. This implies that the non-Gaussianity of the snowpack may not be neglected during the snow accumulation season and late spring season. Interestingly, small ground surface features (e.g., low-centered and high-centered ice wedge polygons) make snow distribution more Gaussian, while snowdrift (snow dunes) on a flat frozen lake seems to be less Gaussian than on tundra or in a drained lake basin.

Our analyses of the ASO SWE products reinforced the findings for snowpacks on the tundra. Although SWE data was chosen instead of snow depth for practical reasons, the common features in non-Gaussianity remain valid. Additionally, the snow diffuser effect of forests was illustrated in three representative areas in the western US. This effect was reported by He et al. (2019) based on airborne LiDAR snow depth measurements on the Snowy Range, Wyoming, USA. Hence, it is likely that vegetation cover generally makes snow distribution more Gaussian in the snow accumulation process; however, further verification of this relationship is recommended.

Overall, a Gaussian distribution is a suitable approximation for snow spatial distribution when the ground is completely covered by snow. Higher-order statistics associated with landscape type may potentially improve the SWE estimation in wind-swept open terrain and near snow lines. The level of non-Gaussianity will determine the choice of statistical tool to correct the systematic bias in snow measurements. Meanwhile, this study suggests the possibility of partitioning the extent of wind-induced snowdrifts by means of independent component analysis (Comon et al., 2010).

Author contribution

NO performed the analysis, and RAPP offered technical advice. NO, ADP, RCR, and BMJ provided the field observed data for the case studies in Alaska. ADP, BMJ, KMH, RAPP, and RCR actively participated in the discussions and manuscript improvement. NO prepared the manuscript with contributions from all co-authors.

Competing interests

The authors declare that they have no conflict of interest.

Acknowledgments

This study was supported by the National Science Foundation (NSF) Office of Polar Programs (OPP) under the awards 1806287, 1806213, and 1806202. The authors thank UIC Science and CH2MHill Polar Field Services (now Battelle Arctic Research Operations) for their logistical field support. RP acknowledges support from the European Union under the Horizon Europe grant 101074004 (C2IMPRESS), the Meteoceanics flagships MR-220617 and MR-070220-BLUE. We used the NSIDC DAAC Airborne Snow Observatory (ASO) data downloaded from NSIDC.org.

Data Availability Statement

The data used in this research are publicly available at the NSF Arctic Data Center: https://doi.org/10.18739/A24746T0K, and https://doi.org/10.18739/A2NV99C4P

References

Aas, K. S., Gisnås, K., Westermann, S., & Berntsen, T. K.: A tiling approach to represent subgrid snow variability in coupled land surface–atmosphere models. *Journal of Hydrometeorology*, *18*(1), 49-63, 2017.

Brubaker, K. L., & Menoes, M. I. C. H. A. E. L.: A technique to estimate snow depletion curves from time-series data using the beta distribution. In *Proceedings of the Eastern Snow Conference* (Vol. 58, pp. 343-346), 2001.

Carter, L. D.: A Pleistocene sand sea on the Alaskan Arctic Coastal Plain. Science, 211(4480), 381–383. https://doi.org/10.1126/science.211.4480.381, 1981.

Comon, P., & Jutten, C. (Eds.): *Handbook of Blind Source Separation: Independent component analysis and applications*. Academic press, 2010.

Comon, P., 1994: Independent component analysis, a new concept? Signal Process., 36, 287–314.

Donald, J. R., Soulis, E. D., Kouwen, N., & Pietroniro, A.: A land cover-based snow cover representation for distributed hydrologic models. *Water Resources Research*, *31*(4), 995-1009, 1995.

Egli, L., & Jonas, T.: Hysteretic dynamics of seasonal snow depth distribution in the Swiss Alps. *Geophysical research letters*, *36*(2), 2009.

Fleming, S. W., Zukiewicz, L., Strobel, M. L., Hofman, H., & Goodbody, A. G.: SNOTEL, the Soil Climate Analysis Network, and water supply forecasting at the Natural Resources Conservation Service: Past, present, and future. JAWRA Journal of the American Water Resources Association, 2023.

498 Hall, D. K., G. A. Riggs, and V. V. Salomonson: MODIS/Terra Snow Cover 5-Min L2 Swath
499   500m. Version 5. Boulder, Colorado USA: NASA National Snow and Ice Data Center
500   Distributed Active Archive Center. http://dx.doi.org/10.5067/ACYTYZB9BEOS, 2006.

501 He, S., Ohara, N., & Miller, S. N.: Understanding subgrid variability of snow depth at 1-km scale
502   using Lidar measurements. *Hydrological Processes*, *33*(11), 1525-1537, 2019.

503 He, S., Smirnova, T. G., & Benjamin, S. G.: Single-Column Validation of a Snow Subgrid
504   Parameterization in the Rapid Update Cycle Land-Surface Model (RUC LSM). *Water*
505   *Resources Research*, *57*(8), e2021WR029955, 2021.

506 Hyvärinen, A., Karhunen, J., & Oja, E.: Independent component analysis and blind source
507   separation. ISBN:9780471221319, |DOI:10.1002/0471221317, John Wiley & Sons, Inc.,
508   2001.

509 Kakalia, Z., Varadharajan, C., Alper, E., Brodie, E., Burrus, M., Carroll, R., ... & Agarwal, D.:
510   The East River Community Observatory Data Collection: Diverse, multiscale data from
511   a mountainous watershed in the East River, Colorado. *Authorea Preprints*, 2020.

512 Kolberg, S. A., & Gottschalk, L.: Updating of snow depletion curve with remote sensing
513   data. *Hydrological Processes: An International Journal*, *20*(11), 2363-2380, 2006.

514 Lalande, M., Ménégoz, M., Krinner, G., Ottlé, C., & Cheruy, F.: Improving climate model skill
515   over High Mountain Asia by adapting snow cover parameterization to complex-
516   topography areas. The Cryosphere, 17(12), 5095-5130, 2023.

517 Liston, G. E.: Representing subgrid snow cover heterogeneities in regional and global
518   models. *Journal of climate*, *17*(6), 1381-1397, 2004.

519 Luce, C. H., & Tarboton, D. G.: The application of depletion curves for parameterization of
520   subgrid variability of snow. *Hydrological processes*, *18*(8), 1409-1422, 2004.

521 Luce, C. H., Tarboton, D. G., & Cooley, K. R.: Sub-grid parameterization of snow distribution
522   for an energy and mass balance snow cover model. *Hydrological Processes*, *13*(12-13),
523   1921-1933, 1999.

524 Meloche, J., Langlois, A., Rutter, N., Royer, A., King, J., Walker, B., ... & Wilcox, E. J.:
525   Characterizing tundra snow sub-pixel variability to improve brightness temperature
526   estimation in satellite SWE retrievals. *The Cryosphere*, *16*(1), 87-101, 2022.

527 Meng, C.: Quantifying the impacts of snow on surface energy balance through assimilating snow
528   cover fraction and snow depth. *Meteorology and Atmospheric Physics*, *129*, 529-538,
529   2017.

530 Mott, R., Daniels, M., & Lehning, M.: Atmospheric flow development and associated changes in
531   turbulent sensible heat flux over a patchy mountain snow cover. *Journal of*
532   *Hydrometeorology*, *16*(3), 1315-1340, 2015.

Mott, R., Schlögl, S., Dirks, L., & Lehning, M.: Impact of extreme land surface heterogeneity on micrometeorology over spring snow cover. *Journal of Hydrometeorology*, *18*(10), 2705-2722, 2017.

Nichols, I.O.: Assessing the accuracy of a UAV snow depth survey Utqiagvik (Barrow), Alaska calm grid, M. S. Thesis, Geological Engineering, Michigan Technological University, 2020.

Nitta, T., Yoshimura, K., Takata, K., O'ishi, R., Sueyoshi, T., Kanae, S., ... & Liston, G. E.: Representing variability in subgrid snow cover and snow depth in a global land model: offline validation. *Journal of climate*, *27*(9), 3318-3330, 2014.

Painter, T. H., Berisford, D. F., Boardman, J. W., Bormann, K. J., Deems, J. S., Gehrke, F., ... & Winstral, A.: The Airborne Snow Observatory: Fusion of scanning lidar, imaging spectrometer, and physically-based modeling for mapping snow water equivalent and snow albedo. *Remote Sensing of Environment*, *184*, 139-152, 2016.

Painter, Thomas H. and Dennis P. Lettenmaier: GPM Ground Validation Airborne Snow Observatory (ASO) OLYMPEX [indicate subset used]. Dataset available online from the NASA Global Hydrometeorology Resource Center DAAC, Huntsville, Alabama, U.S.A. DOI: http://dx.doi.org/10.5067/GPMGV/OLYMPEX/LIDAR/DATA101, 2018.

Pires, C.A., and R.A.P. Perdigão: Non-Gaussianity and Asymmetry of the Winter Monthly Precipitation Estimation from the NAO. Mon. Wea. Rev., 135, 430–448, https://doi.org/10.1175/MWR3407.1, 2007.

Perdigão, R.A.P.: Nonlinear statistics and dynamics of atmospheric predictability and downscaling. http://hdl.handle.net/10451/2013, 2010.

Perdigão, R.A.P.: Fluid Dynamical Systems: From Quantum Gravitation to Thermodynamic Cosmology. https://doi.org/10.46337/mdsc.5091, 2017.

Perdigão, R.A.P.: Polyadic Entropy, Synergy and Redundancy among Statistically Independent Processes in Nonlinear Statistical Physics with Microphysical Codependence. Entropy 2018, 20, 26. https://doi.org/10.3390/e20010026, 2018.

Rudisill, William, Alan Rhoades, Zexuan Xu, and Daniel R. Feldman: Are atmospheric models too cold in the mountains? The state of science and insights from the SAIL field campaign. *Bulletin of the American Meteorological Society*, 2024.

Rangel, R. C., Ohara, N., Parsekian, A. D., and Jones, B. M.: Arctic Tundra Lake Drainage Increases Snow Storage in Drifts. *Journal of Geophysical Research: Earth Surface*, e2023JF007294, 2023a.

Rangel, R. C., Parsekian, A. D., Ohara, N., and Jones, B. M.: Ground Penetrating Radar (GPR) data on snow over lakes and drained lake basins in Inigok, North Slope of Alaska, April 2019. Arctic Data Center. doi:10.18739/A2NV99C4P, 2023b.

Santanello Jr, J. A., Dirmeyer, P. A., Ferguson, C. R., Findell, K. L., Tawfik, A. B., Berg, A., ... & Wulfmeyer, V.: Land–atmosphere interactions: The LoCo perspective. *Bulletin of the American Meteorological Society*, *99*(6), 1253-1272, 2018.

Sengupta, A., Singh, B., DeFlorio, M. J., Raymond, C., Robertson, A. W., Zeng, X., ... & Jones, J.: Advances in subseasonal to seasonal prediction relevant to water management in the western United States. Bulletin of the American Meteorological Society, 103(10), E2168-E2175, 2022.

Shamir, E., & Georgakakos, K. P.: Estimating snow depletion curves for American River basins using distributed snow modeling. *Journal of Hydrology*, *334*(1-2), 162-173, 2007.

Skaugen, T., & Randen, F.: Modeling the spatial distribution of snow water equivalent, taking into account changes in snow-covered area. *Annals of Glaciology*, *54*(62), 305-313, 2013.

Sturm, M., & Holmgren, J.: An automatic snow depth probe for field validation campaigns. Water Resources Research, 54(11), 9695-9701, 2018.

Tarricone, J., Webb, R. W., Marshall, H. P., Nolin, A. W., & Meyer, F. J.: Estimating snow accumulation and ablation with L-band interferometric synthetic aperture radar (InSAR). *The Cryosphere*, *17*(5), 1997-2019, 2023.

Tsang, L., Durand, M., Derksen, C., Barros, A. P., Kang, D. H., Lievens, H., ... & Xu, X.: Global monitoring of snow water equivalent using high-frequency radar remote sensing. *The Cryosphere*, *16*(9), 3531-3573, 2022.

Younas, W., Hay, R. W., MacDonald, M. K., ul ISLAM, S., & Dery, S. J.: A strategy to represent impacts of subgrid-scale topography on snow evolution in the Canadian Land Surface Scheme. *Annals of Glaciology*, *58*(75pt1), 1-10, 2017.